

Article

Flow Stress Behavior and Microstructure Evolution of Austenitic Stainless Steel with Low Copper Content during Hot Compression Deformation

Huaying Li ^{1,*}, Lihong Gao ¹, Yaohui Song ¹, Lidong Ma ^{2,*}, Haitao Liu ^{3,*}, Juan Li ² and Guanghui Zhao ²

¹ School of Materials Science and Engineering, Taiyuan University of Science and Technology, Taiyuan 030024, China; sitglh@163.com (L.G.); syhty96@163.com (Y.S.)

² Coordinative Innovation Centre of Taiyuan Heavy Machinery Equipment, Taiyuan University of Science and Technology, Taiyuan 030024, China; 2021019@tyust.edu.cn (J.L.); zghjx@tyust.edu.cn (G.Z.)

³ State Key Laboratory of Rolling and Automation, Northeastern University, Shenyang 110819, China

* Correspondence: 2014246@tyust.edu.cn (H.L.); 2010007@tyust.edu.cn (L.M.); liuht@ral.neu.edu.cn (H.L.)

Abstract: In order to study the microstructure evolution and flow stress behavior of as cast antibacterial austenitic stainless steel containing 1.52 wt.% copper, Gleeble 3800 was used for thermal compression simulation test. Through OM and EBSD analysis, it is found that the dynamic recrystallization mechanism of thermal deformation is mainly discontinuous dynamic recrystallization. With the increase of deformation temperature and deformation rate, the proportion of recrystallization nucleation gradually increases. The growth of twins relies on recrystallization and, at the same time, promotes dynamic recrystallization. Considering the influence of strain on flow stress, the strain compensation Arrhenius model is established according to the obtained stress-strain curve, and high accuracy is obtained. The correlation coefficient and average relative absolute error are 0.979 and 7.066% respectively. These results provide basic guidance for the technology of microstructure control and excellent mechanical properties of antibacterial stainless steel.

Keywords: austenitic stainless steel; dynamic recrystallization; hot compression; hot deformation behavior



Citation: Li, H.; Gao, L.; Song, Y.; Ma, L.; Liu, H.; Li, J.; Zhao, G. Flow Stress Behavior and Microstructure Evolution of Austenitic Stainless Steel with Low Copper Content during Hot Compression Deformation. *Crystals* **2021**, *11*, 1408. <https://doi.org/10.3390/cryst11111408>

Academic Editors: Pavel Lukáč and Umberto Prisco

Received: 25 October 2021

Accepted: 13 November 2021

Published: 18 November 2021

Publisher's Note: MDPI stays neutral with regard to jurisdictional claims in published maps and institutional affiliations.



Copyright: © 2021 by the authors. Licensee MDPI, Basel, Switzerland. This article is an open access article distributed under the terms and conditions of the Creative Commons Attribution (CC BY) license (<https://creativecommons.org/licenses/by/4.0/>).

1. Introduction

Antibacterial stainless steels are widely used for artificial joints, kitchen tableware, food industry, heart stent and so on [1,2]. Compared with light metals, Cu bearing antibacterial stainless steel is a kind of most frequently applied antibacterial stainless steels, mainly due to its excellent combination of good mechanical properties, exceptional durable performances, and manufacturing process [3–6]. Cu precipitation is the key to obtain antimicrobial ability of stainless steel. Some related works [7] indicated there were Cu precipitations observed in the antibacterial stainless steels by transmission electron microscopy. The mean size of Cu precipitations appeared especially small, with the content of Cu in the chemical composition is as high as 80%. Moreover, the addition of Cu can prevent recovery and recrystallization softening and suppress grain growing up for the pinning effect by forming ϵ -Cu phase. Cu ions dissolved from the surface of stainless steel can destroy the protein structure in bacteria, inhibit the replication of bacterial DNA and the synthesis of related proteins/enzymes, destroy the metabolic activities in bacteria, make bacteria inactive and lead to bacterial death [8]. Therefore, the bactericidal rate increases with the increase of Cu content, and the killing time decreases with the increase of Cu content. However, “Cu embrittlement” will happen when the Cu content is over 0.35 wt.%, which can restrict the industrial production of antibacterial stainless-steel [9]. It is well known that deformation behavior of the steels greatly relies on various factors in hot working [10–16]. Proper Cu content is still controversial for the favorable thermal deformation behavior because the thermal deformation behavior is different for different

Cu contents. Therefore, the deformation behavior of steel with Cu addition is needed to be studied.

When the Cu content of 0.5~4 wt.% is added to stainless steel, good antibacterial properties can be obtained after heat treatment. At present, the hot working of antibacterial austenitic stainless steel (3.6 wt.% Cu and 2.42 wt.% Cu) has been studied in the literature, the constitutive equation has been established, and the microstructure change law of hot working has been analyzed [17–19]. However, there are few studies on economical antibacterial austenite stainless steel with low Cu content. Thermal deformation is an important way to explore its forming properties, and the constitutive model can better reflect its rheological behavior. In addition, with the increase in research on the hot deformation behavior of austenitic stainless steels with different copper content, machine learning has made major breakthroughs in materials, and the application of these technologies is of great significance for optimizing the copper ratio [20–24].

It has been widely confirmed that thermomechanical processing is an effective technology to control microstructure and obtain excellent mechanical properties by optimizing thermal deformation parameters, such as temperature and strain rate. Therefore, a systematic work of 304 L stainless steel with 1.52 wt.% Cu- under various processing conditions have been conducted. In addition, the microstructure and flow stress curves will be investigated based on the microstructure characterization and constitutive equation.

2. Experimental

The tested material consisted of components as given in Table 1, which is electro-slag remelted stainless steel ingots with 1.52 wt.% Cu addition. Compression samples are made into round bars, 10 mm in diameter and 15 mm in length. Thermal simulation tests were carried out with a compression deformation of 50% using Gleeble 3800 (DSI, Tucker, GA, USA). Heat the sample at 10 °C/s to 1250 °C and hold it for 5 min, then separately cooled to 900~1150 °C (at 50 °C intervals), followed by loading at corresponding strain rates (0.01, 0.1, 1, 2.5, 5, 10, 20 s⁻¹), finally arrived at room temperature with a drop speed of 50 °C/s (as shown in Figure 1). Microstructural observations were performed using the Zeiss optical microscope (OM) and the electron backscatter diffraction (EBSD) (Oxford, UK). Corrosion of OM samples were performed by 10% oxalic acid after standard mechanical polishing. Electropolishing of EBSD samples with perchloric acid alcohol were implemented.

Table 1. Chemical composition (wt.%) of Cu bearing antiseptic stainless steel.

C	Si	Mn	P	S	Cr	Ni	Cu
0.003	0.44	1.54	0.009	0.001	18.05	8.50	1.52

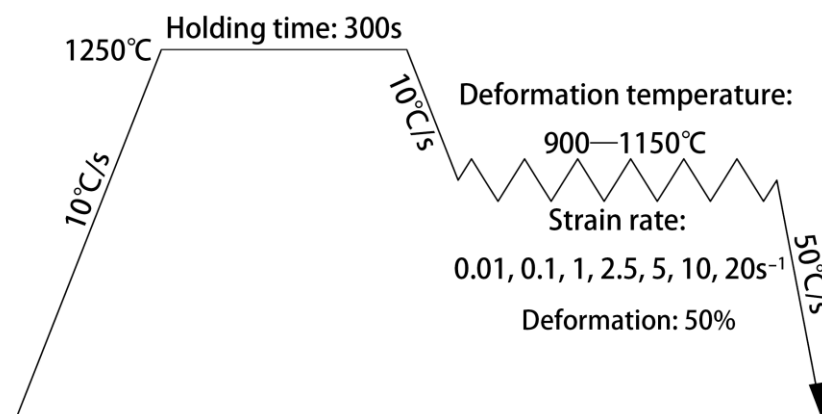


Figure 1. Schematic diagram of thermal deformation process.

3. Results and Discussions

3.1. Microstructure

Figure 2 exhibits the microstructure of Cu bearing-antiseptic stainless steel as a function of deformation temperature. At 900 °C, the microstructure presented an elongated feature, and the recrystal grains were hardly found (Figure 2a). Lots of recrystal grain appears at the original grain boundary at 1000 °C, which indicates the occurrence of dynamic recrystallization (DRX) (Figure 2b). A large number of annealing twins and equiaxed grains existed at 1100 °C, which may be related to the reason that the higher deformation temperatures increase grain boundary migration ability and promote not only nucleating but also growing up of dynamic recrystallisation [25].

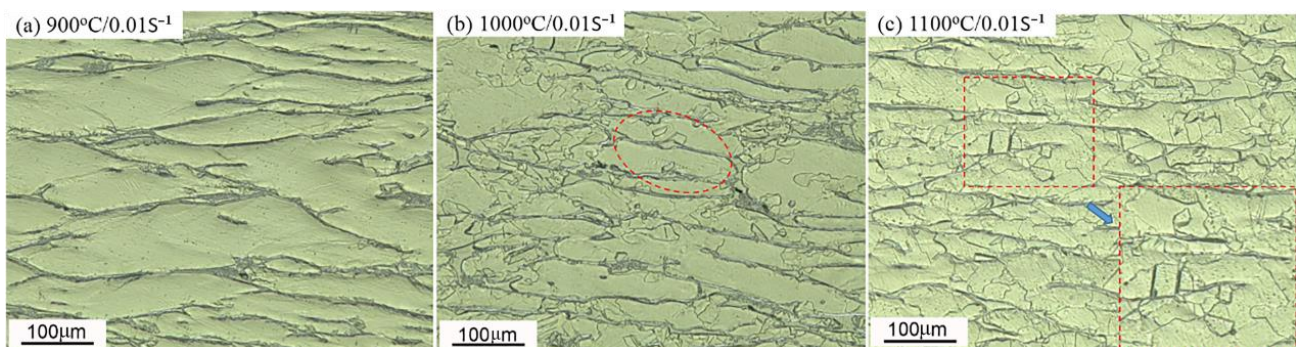


Figure 2. Microstructures of austenitic stainless steel with 1.52 wt. % Cu at 0.01 s^{-1} for different deformation temperatures (a) 900 °C; (b) 1000 °C; (c) 1100 °C.

From Figure 3, the increase in the deformation rate leads to more recrystallized grains and enhanced grain refinement at 1000 °C. The grain size presents uneven when the deformation rate is 1 s^{-1} . From Figure 3b, the increase of dislocation density, driving force of DRX, and recrystallization nucleation position will result in grain refinement. These factors affect the formation of more twins simultaneously [26]. A majority of the recrystallization grains comprises twins at high rate, as shown in Figure 3c. According to previous studies, higher energy storage will be generated at high rate, which promotes the nucleation of twins and the rapid expansion of DRX region [27].

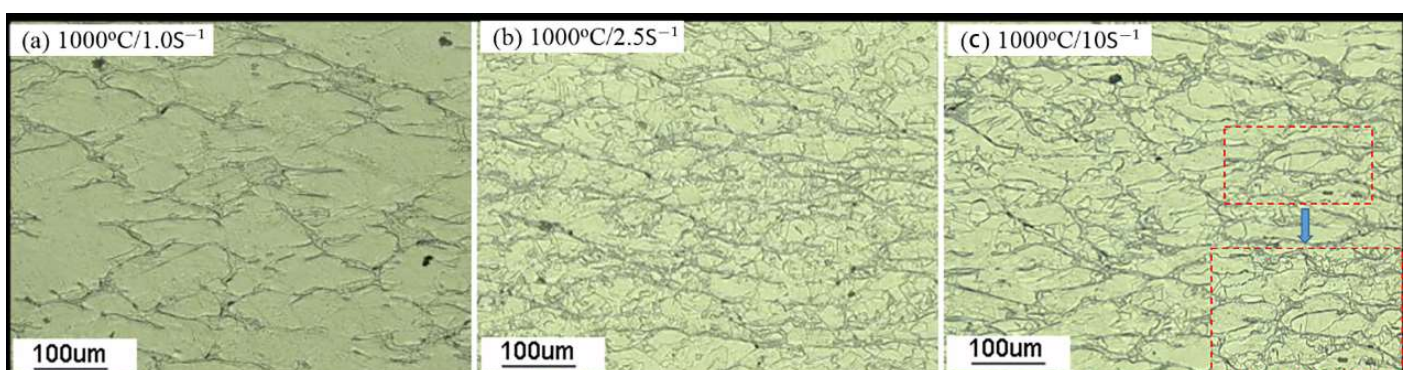


Figure 3. Microstructures of austenitic stainless steel with Cu-1.52% at 1000 °C for different strain rates (a) 1.0 s^{-1} ; (b) 2.5 s^{-1} ; (c) 10 s^{-1} .

Figure 4 further shows the microstructure evolution of EBSD. The grain boundaries present serrated feature, which will become the potential nucleation sites at low temperatures. It can be seen the nucleation and recrystallization take place at original grains boundaries, from the enlarged Figure 4a. At 1150 °C, most of the grain boundaries have not only recrystallized grains but also containing twins, and the grains grow significantly, as shown in Figure 4b. According to EBSD statistical results (Figure 5), the proportion of

the twins is higher with the increase of the strain rates. M. Azarbarmas [28] also reported that twins emerged in the course of recrystallized grains growing up.

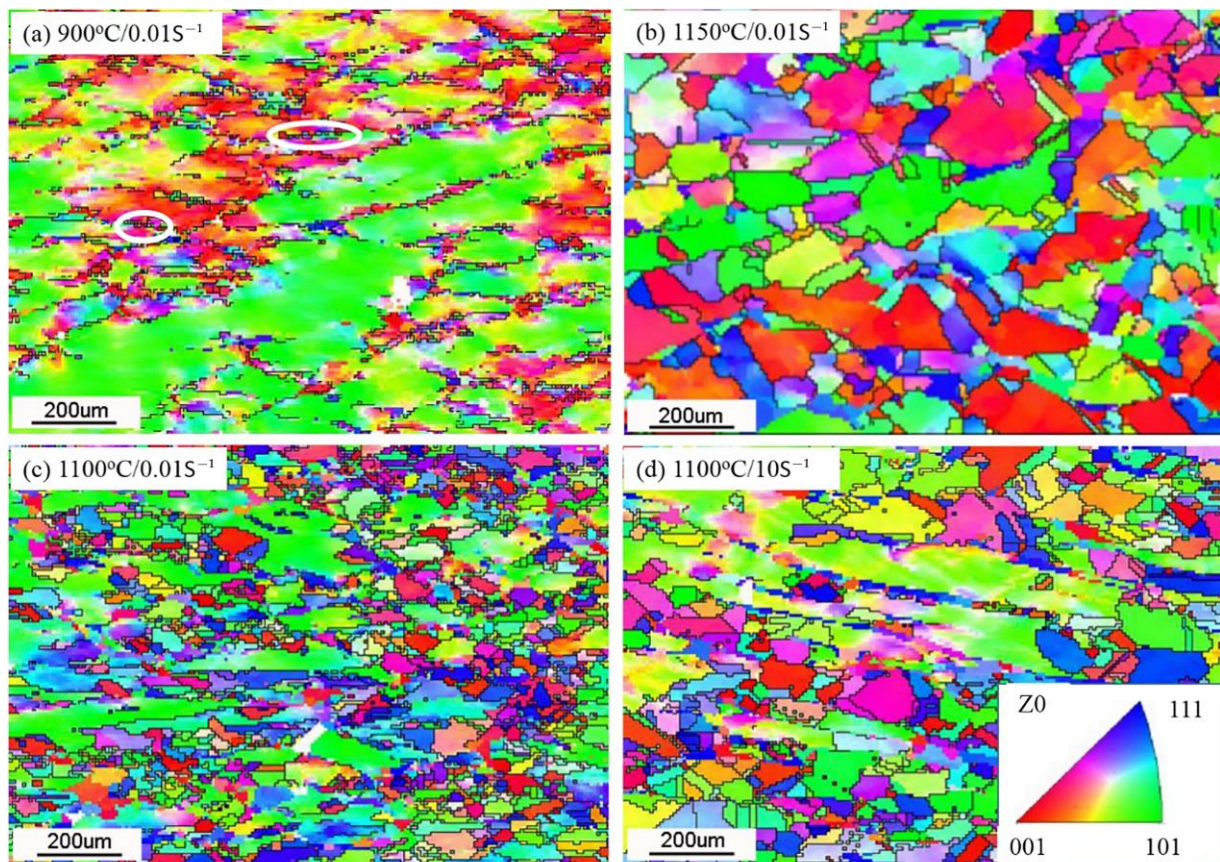


Figure 4. EBSD of austenitic stainless steel with Cu-1.52% (a) 900 °C/0.01 s⁻¹; (b) 1150 °C/0.01 s⁻¹; (c) 1100 °C/0.01 s⁻¹; (d) 1100 °C/10 s⁻¹.

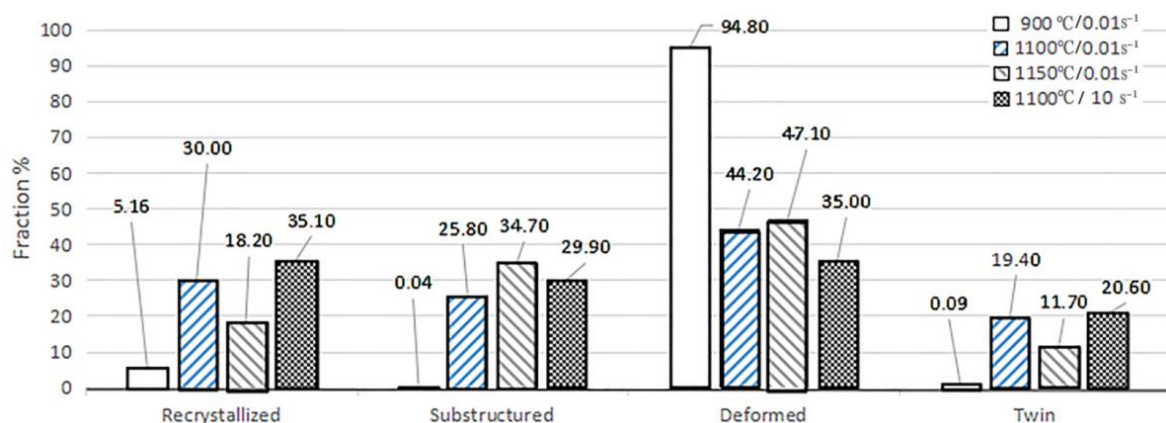


Figure 5. The fraction of recrystallized, substructured, deformed microstructure and twin of austenitic stainless steel with Cu-1.52% in different condition.

Based on the results presented in Figure 4c, it is obviously the nucleation driving force is small because of the higher temperature (1100 °C) and lower strain rate (0.01 s⁻¹), and the deformed grain reaches to 44.20%, but the degree of recrystallization is only 30.00% (Figure 5). As the strain rate increases up to 10 s⁻¹ (Figure 4d), the dislocation density and driving force are higher, and the degree of recrystallization increase up to 35.10%. However, the recrystallization nucleation is less, and the fine recrystallization grains appears due

to the short deformation time. In addition, recrystallization grain appeared at higher temperature. The proportion of twins were higher since deformation temperatures and strain rates rise (Figure 5). The energy of the growing grain boundaries is reduced by twins. The twinning can adjust the orientation of the grains and release the energy storage in the alloy, which stimulates more new slip systems. In addition, the twins can promote DRX, and consume deformation stores energy. Therefore, the twins can make the grains refinement and increase the ductility of the alloy [29].

The internal orientation is relatively simple at the low strain rates during thermal deformation, and most of orientations are $\langle 001 \rangle$ and $\langle 101 \rangle$, which are agreement with the previous studies [18]. As shown in Figure 4b–d, the deformation texture occurs with the recrystallization texture simultaneously. The grain orientation changes gradually with the occurrence of DRX. Twins and the microstructure interior distributed randomly. Finally, most of the banded grains are mainly $\langle 101 \rangle$ orientation.

The sub-grain boundary transition can be investigated by analyzing the orientation difference using EBSD, and then the recrystallization deformation mechanism can be studied. It can be seen from Figure 6a, when the temperature is $900\text{ }^{\circ}\text{C}$ and the strain rate is 0.01 s^{-1} , the value of average orientation difference is 12.5° . The orientation difference is mainly concentrated between $0\text{--}15^{\circ}$ and distributed continuously. It can be inferred that most of the microstructures are sub-grain boundaries. It is well known that the deformation mechanism of austenitic steel is mainly dislocation slip [30]. At low strain rate, the grains are mainly composed of sub-grains with small angle grain boundaries and a variety of dislocation structures.

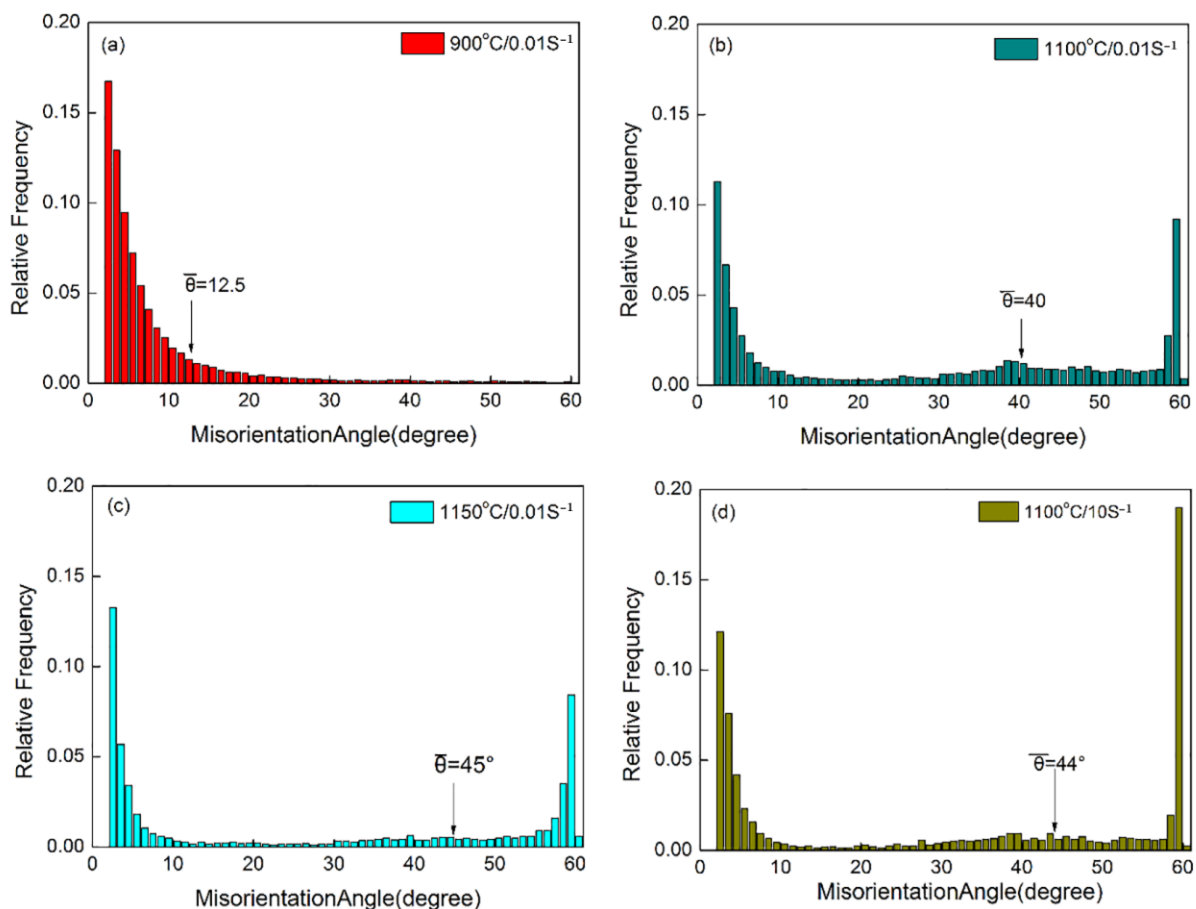


Figure 6. Grain boundary misorientation distribution plots at various reduction rates. (a) $900\text{ }^{\circ}\text{C}/0.01\text{ s}^{-1}$; (b) $1100\text{ }^{\circ}\text{C}/0.01\text{ s}^{-1}$; (c) $1150\text{ }^{\circ}\text{C}/0.01\text{ s}^{-1}$; (d) $1100\text{ }^{\circ}\text{C}/10\text{ s}^{-1}$.

During the classic continuous DRX, the sub-boundary will transform into a large-angle interface under a certain accumulation of deformation through increasing orientation difference [31]. The misorientation distribution displays as a typical bimodal type $<10^\circ$ and $50\sim 60^\circ$ with increase of deformation temperature from 1100°C to 1150°C , therefore the dominant recrystallization mechanism is discontinuous dynamic recrystallization. The atom diffusion ability and crystal boundary migration sharply increase with the increase in temperatures. The growth of recrystallization grains leads to the increase in the difference of the orientation of large-angle grain boundaries (Figure 6b–d). The increase in strain rate increases the distortion energy at 1000°C . Therefore, the twins increase and the proportion of 60° orientation difference increases from 0.1% to 0.19% for the 304 stainless steel, with a lower stacking-fault energy.

3.2. The Deformation Behaviors during Hot Deformation

3.2.1. Effect of Recrystallization on Deformation Behavior

It can be seen from Figure 7 that the stainless steel under test exhibits work hardening firstly and then softening during hot compression deformation. The dislocation density increases at the initial deformation stage. At this stage, the samples exhibit obvious work-hardening, and flow stress increases rapidly. Then flow stress increase slowly, which may be related to the increased internal energy. The dislocations rearrangement occurs to some degree and produces sub-crystals, resulting in the slower enhancement of dislocation density and the increasement of dynamic recovery (DRV) softening.

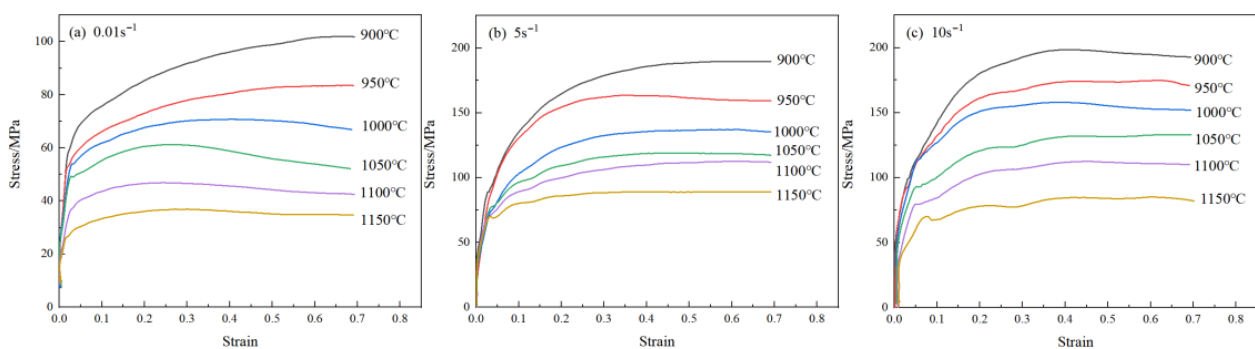


Figure 7. The stress-strain curves of antimicrobial austenitic stainless steel with Cu-1.52% for different temperatures during hot compression (a) 0.01 s^{-1} , (b) 5 s^{-1} , (c) 10 s^{-1} .

The rapid recrystallization nucleation of a material with a lower dislocation energy hardly happens. The stage, shown in Figure 7, is mainly work hardening with the softening mechanism of dynamic recovery, such as $900^\circ\text{C}/0.01\text{ s}^{-1}$, and rheological stress keeps increasing when strain enhances in this stage. The other parts of curve present a small peak and the material undergoes dynamic recrystallization and softening behavior. The curve tends to be horizontal when the offset is achieved between softening and work hardening behavior. For example, it can be deduced that the curves for $1100^\circ\text{C}/0.01\text{ s}^{-1}$ show complete recrystallization and the equiaxed microstructures are uniformly distributed. Atomic motion is accelerated with deformation temperatures rising at a certain strain rate, and which can cause the flow stress and peak stress decrease with the increases in temperature. The atomic heat activation energy increases with the increase in temperature, which will promote the slip and climbing of dislocation. In addition, the stress reaches the peak quickly with increase in strain rate in Figure 7. Softening and offset of the deformation resistance cannot be fully carried out due to the time famine for dynamic recrystallization and recovery. The stress is higher due to the longer time continuous work hardening after stabilization. The rheological curves exhibit typical dynamic recovery features at high strain rates. Based on the statistical chart shown in Figure 5, it can be seen that the recrystallization is only 30% at low strain rate. The driving force and position of

recrystallization nucleation increase with strain rate, which result in an increase in grain recrystallization degree from 30.00% to 35.10%.

Normally, DRV benefits the hot working performance in a particular range of processing parameters during thermal deformation [32,33], and so is DRX. The strain rates were preset to be at the range of 0.01~20 s⁻¹ in the experiments. Equations (1) and (2) are usually used to calculate the temperature rise caused by deformation [34].

$$\Delta T = (0.95\eta/\rho C_p) \int_0^\epsilon \sigma d\epsilon \quad (1)$$

$$\eta = (0.316)\lg\dot{\epsilon} + 0.95 \quad (2)$$

where, C_p stands for the specific heat, and its value is selected according to the published papers [35]; η is the thermal efficiency, obtained by Equation (2) [36]; ρ is 7.94 g/mm³, the density of the material.

The heat transformation changes from isothermal to adiabatic during the thermal deformation and the increase of equivalent strain rate will affect the flow stress. The deformation heat effect cannot be ignored.

The contour of temperature rise at different rates and temperatures is given in Figure 8a. The value of temperature rises when the temperature increases and the stress decreases. The rheological curves cannot require any correction for the neglect of adiabatic heating due to long-term deformation at lower strain rates [37,38]. The maximum value of temperature rises from 1 °C to 24 °C. The difference between the measured value and the isotherm caused by the rapid increase of deformation heat research maximum at a high strain rate. Therefore, the stress-strain curves are corrected when strain rates are greater than 1 s⁻¹. Then, the constant value (σ_2) in $T_0 + \Delta T$ has been used to represent the uncorrected value (σ_1) in T_0 . The correction can be seen from the fitted line (Figure 9b), and the stress value can be expressed by Equation (3) [36].

$$\sigma_2(T_0) \Big|_{\dot{\epsilon}\dot{\epsilon}} \approx \sigma_1(T_0) \Big|_{\dot{\epsilon}\dot{\epsilon}} - \sigma'_2(T_0) \Big|_{\dot{\epsilon}\dot{\epsilon}} \cdot \Delta T \quad (3)$$

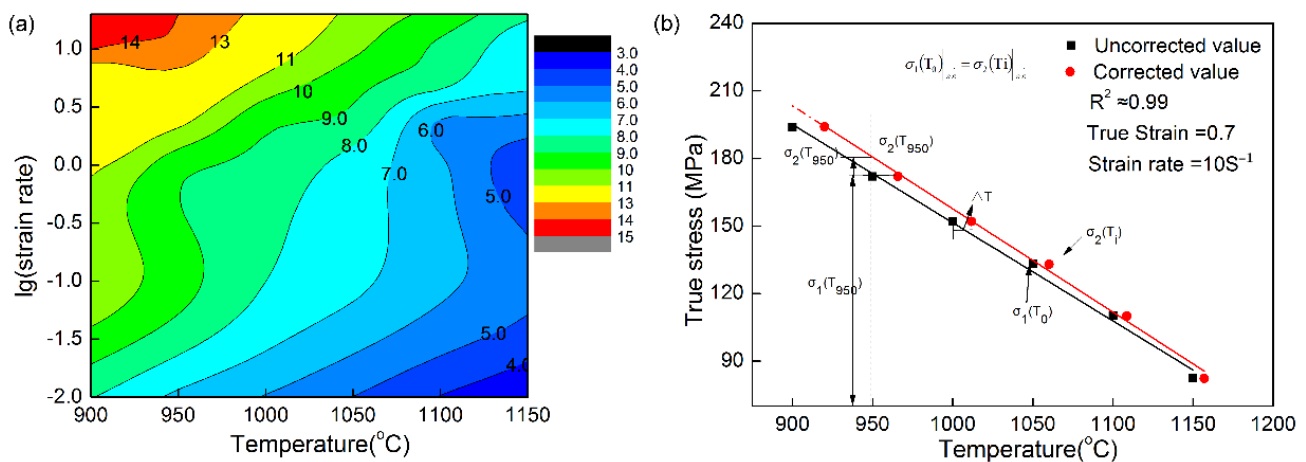


Figure 8. (a) Contour plot of temperature rise at a strain of 0.7, (b) σ - T at 0.7 for a strain rate of 10 s⁻¹.

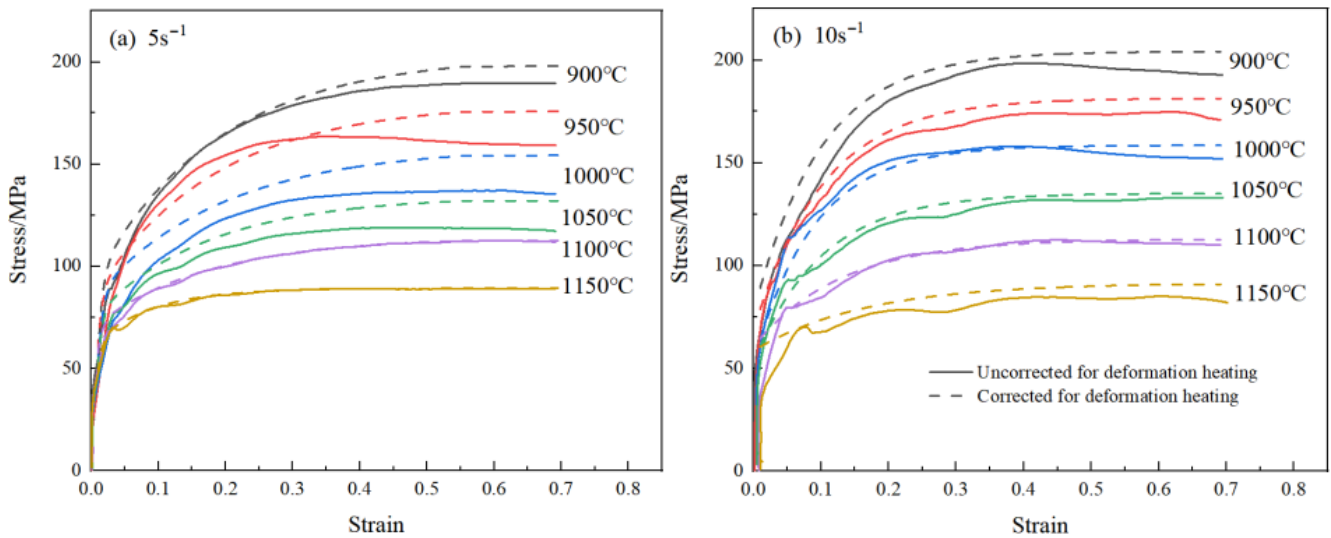


Figure 9. The corrected true strain-strain curves of antimicrobial austenitic stainless steel with Cu-1.52% at different temperatures (a) 5 s^{-1} , (b) 10 s^{-1} .

The curves of true stress-strain of antibacterial stainless-steel with 1.52 wt. % Cu during thermal simulation compression process by using various temperatures have been available at Figure 9. Flow stress curves (dotted lines in the Figure 9) are obtained based on the above formula. Apparently, the deformation temperature has important effects on the flow stress, especially for high-rate thermal deformation.

3.2.2. Hot Deformation Constitutive Equation

There are many factors that affect the thermal deformation behavior of metal materials. Among various flow stress curve equations, the classical Arrhenius relation is in good agreement with the flow stress behavior of Cu bearing stainless steel [39,40]:

$$\dot{\varepsilon} = A[\sinh(\alpha\sigma)]^n \exp(-Q/RT) \quad (4)$$

$$Z = \dot{\varepsilon} \exp\left(\frac{Q}{RT}\right) = A[\sinh(\alpha\sigma)]^n \quad (5)$$

In the formula, the activation energy of hot deformation is expressed by the letter Q (kJ/mol); α , A are the material factors; R represents a universal gas constant (8.314 J/(mol·K)); n is called stress exponent; Zener-Hollomon parameter (z) is temperature dependent and compensates for the strain rate factor, independent of α . Substituting the two sides of Equation (5):

$$\ln[\sinh(\alpha\sigma_p)] = \frac{1}{n} \ln \dot{\varepsilon} + \frac{Q}{nRT} - \frac{\ln A}{n} \quad (6)$$

Multiply linear regression was performed to analyze the peak stress data of the true stress-strain curves when strain rates changing and various temperatures, which was measured by the least squares method, and α was 0.00998. As shown in Figure 10a, the slope calculated by plotting $\ln[\sinh(\alpha\sigma_p)]$ remains unchanged with temperature variations, in addition, Z and the peak stress increases with the enhancement of strain rates step by step (Figure 10c). As shown in Figure 10b, the peak stress increases when deformation temperature decreasing. The average slope and intercept were obtained from the linear regression lines, and $n = 6.56$, $Q = 421635.0315 \text{ J/mol}$, $A = 1.27 \times 10^{16}$, respectively. Therefore, based on the above data, the constitutive equation for austenitic stainless steel with 1.52% Cu addition can be expressed as the following equations:

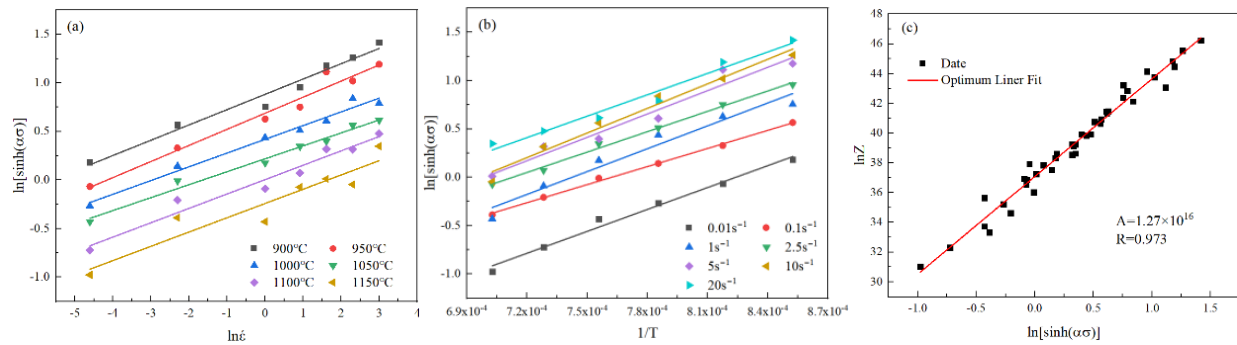


Figure 10. Relationships between (a) $\ln[\sinh(\alpha\sigma)] - \ln \dot{\varepsilon}$; (b) $\ln[\sinh(\alpha\sigma)] - 1000/T$; (c) $\ln[\sinh(\alpha\sigma)] - \ln Z$.

$$\dot{\varepsilon} = 1.27 \times 10^{16} [\sinh(0.00998\sigma)]^{6.56} \exp\left(\frac{-421635.0315}{RT}\right) \quad (7)$$

$$Z = \dot{\varepsilon} \exp\left(\frac{421635.0315}{RT}\right) = 1.27 \times 10^{16} [\sinh(0.00998\sigma)]^{6.56} \quad (8)$$

Equation (7) can be rewritten as a hyperbolic sine function equation:

$$\sigma = \frac{1}{0.00998} \ln \left\{ \left(\frac{Z}{1.27 \times 10^{16}} \right)^{\frac{1}{6.56}} + \left[\left(\frac{Z}{1.27 \times 10^{16}} \right)^{\frac{2}{6.56}} + 1 \right]^{\frac{1}{2}} \right\} \quad (9)$$

However, the above equation does not consider the effect of strain on flow stress during high-temperature deformation. To better predict the flow stress of the material in this study, a constitutive equation is established every 0.1 strain in the 0.1–0.9 strain, and the α , n , Q and $\ln A$ under different strains are calculated. Assuming that the material constant and thermal activation energy are based on the polynomial functions of strain, the five-order polynomial fitting shows better accuracy through polynomial fitting. The fitting of each parameter is shown in Figure 11. It is found that α , n , Q and $\ln A$ exhibit obvious changes to different strains. The coefficients of the polynomial function Equation (10) are shown in Table 2.

$$\begin{cases} \sigma = \frac{1}{\alpha} \ln \left\{ \left(\frac{Z}{A} \right)^{\frac{1}{n}} + \left[\left(\frac{Z}{A} \right)^{\frac{2}{n}} + 1 \right]^{\frac{1}{2}} \right\} \\ Z = \dot{\varepsilon} \exp\left(\frac{Q}{RT}\right) \\ \alpha = a_0 + a_1\varepsilon + a_2\varepsilon^2 + a_3\varepsilon^3 + a_4\varepsilon^4 + a_5\varepsilon^5 \\ n = n_0 + n_1\varepsilon + n_2\varepsilon^2 + n_3\varepsilon^3 + n_4\varepsilon^4 + n_5\varepsilon^5 \\ Q = Q_0 + Q_1\varepsilon + Q_2\varepsilon^2 + Q_3\varepsilon^3 + Q_4\varepsilon^4 + Q_5\varepsilon^5 \\ \ln A = A_0 + A_1\varepsilon + A_2\varepsilon^2 + A_3\varepsilon^3 + A_4\varepsilon^4 + A_5\varepsilon^5 \end{cases} \quad (10)$$

Table 2. Coefficients of the polynomial equations in Equation (10).

	α	n	Q	$\ln A$			
a_0	0.01364	n_0	7.20089	Q_0	177857.4301	A_0	16.31829
a_1	−0.03141	n_1	−2.7189	Q_1	3009200	A_1	257.78717
a_2	0.13479	n_2	−3.13846	Q_2	−15454900	A_2	−1333.17329
a_3	−0.3247	n_3	16.2329	Q_3	37634900	A_3	3256.41102
a_4	0.39356	n_4	−12.16705	Q_4	−43657000	A_4	−3771.69205
a_5	−0.18333	n_5	−2.17917	Q_5	19264800	A_5	1656.975

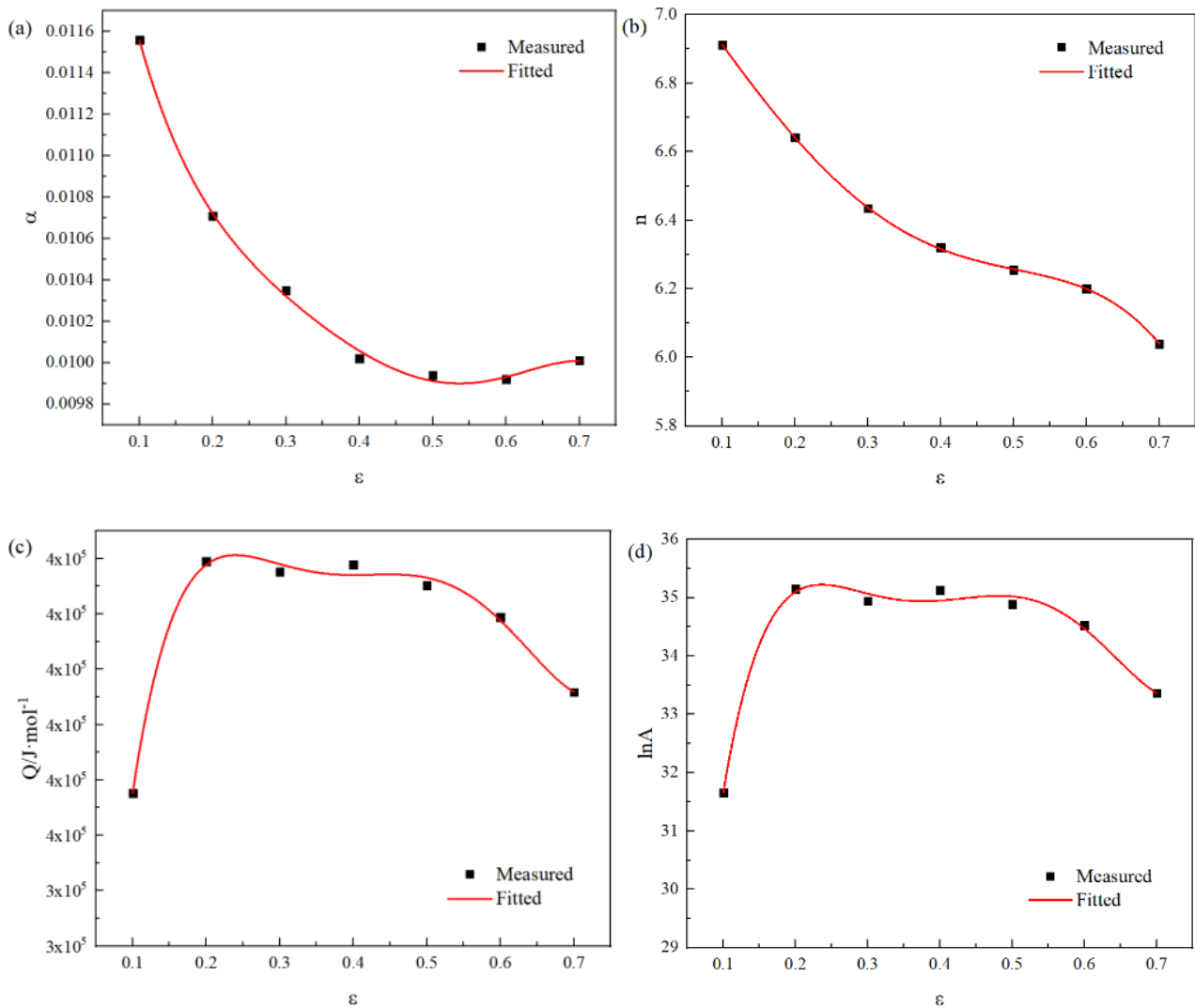


Figure 11. Relationships between strain and: (a) α ; (b) n ; (c) Q ; (d) $\ln A$.

Figure 12 shows the experimental and predicted values of flow stress under different deformation conditions. It can be found that the predicted values are in good agreement with the experimental values. The correlation coefficient (R) and the average absolute relative error ($AARE$) are employed to illustrate the accuracy of the constitutive equation. The equations for the calculation of R and $AARE$ are expressed as [41]:

$$R = \frac{\sum_{i=1}^N (E_i - \bar{E})(P_i - \bar{P})}{\sqrt{\sum_{i=1}^N (E_i - \bar{E})^2 \sum_{i=1}^N (P_i - \bar{P})^2}} \quad (11)$$

$$AARE = \frac{1}{N} \sum_{i=1}^N \left| \frac{E_i - P_i}{E_i} \right| \times 100\% \quad (12)$$

where E refers to the experimental data, P represents the predicted data, \bar{E} and \bar{P} denote the average values, and N is the number of data points.

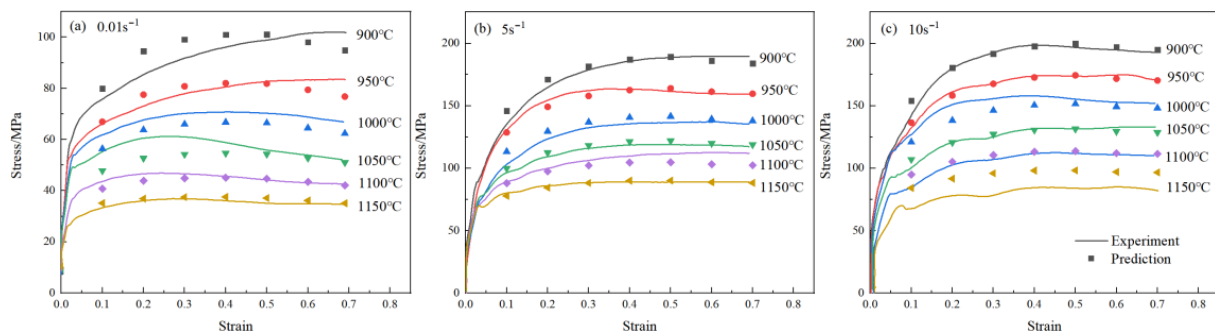


Figure 12. Comparison between experimental values and predicted values (a) 0.01 s^{-1} , (b) 5 s^{-1} , (c) 10 s^{-1} .

Figure 13 shows that a good linear relationship exists between the experiment and the prediction. The correlation coefficient R is 0.979, and the $AARE$ is 7.066%, which further shows that the constitutive equation has a better predictive ability for the flow stress of the alloy.

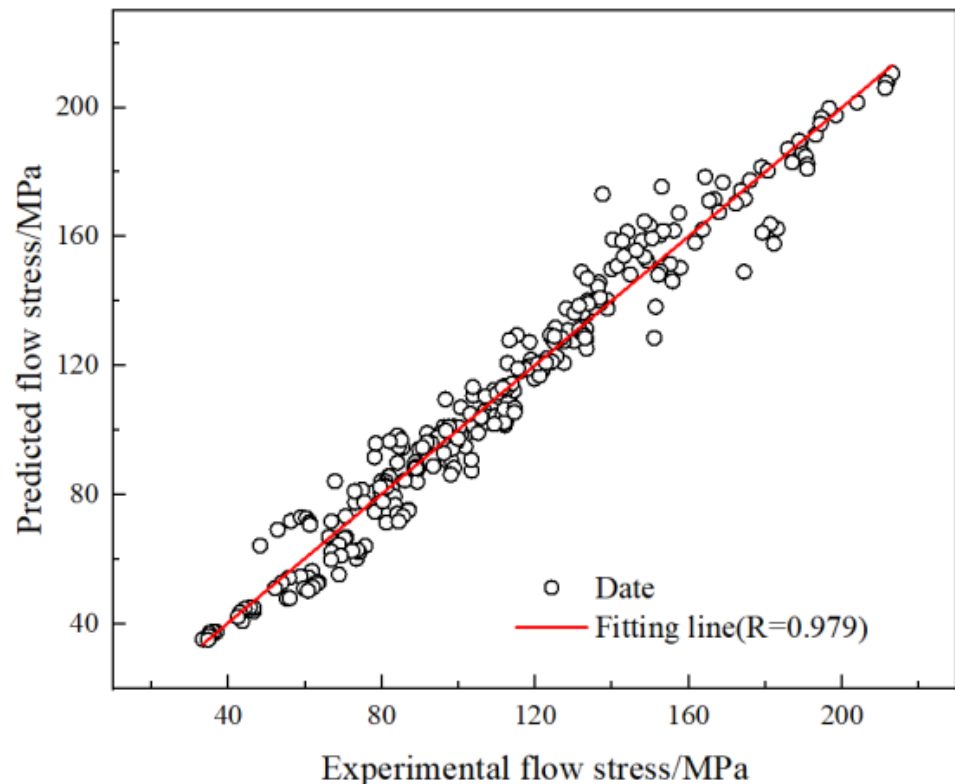


Figure 13. Correlation between experimental and strain-compensated predicted flow stresses.

4. Conclusions

In this paper, the hot deformation behavior of 1.52 wt.% Cu austenitic stainless steel under the deformation conditions of $0.01\text{--}20 \text{ s}^{-1}$ and $900\text{--}1150 \text{ }^\circ\text{C}$ is studied. The microstructure changes under different deformation conditions are analyzed, and the strain compensation Arrhenius constitutive model is constructed. The results are as follows:

- (1) The ratio of recrystallization nucleating sites, located in the twin boundaries, is higher when the strain rates are increasing. The twins depend on recrystallization and promote dynamic recrystallization. The dynamic recrystallization mechanism of thermal deformation is mainly discontinuous dynamic recrystallization.

- (2) The adiabatic temperature rise increases with the decrease of temperature and the increase of strain rate. By modifying the stress-strain curve, the influence of adiabatic temperature rise at high rate ($\geq 1 \text{ s}^{-1}$) is eliminated.
- (3) The constitutive equation of peak stress is established through kinetic analysis as follows.

$$\dot{\varepsilon} = 1.27 \times 10^{16} [\sinh(0.00998\sigma)]^{6.56} \exp\left(\frac{-421635.0315}{RT}\right)$$

$$Z = \dot{\varepsilon} \exp\left(\frac{421635.0315}{RT}\right) = 1.27 \times 10^{16} [\sinh(0.00998\sigma)]^{6.56}$$

In addition, a strain compensation model based on Arrhenius model was established. The calculated values of correlation coefficient R and $AARE$ are 0.979 and 7.066%, respectively when fitting the experimental and predicted results, indicating that the model is accurate and available to better predict the flow stress.

Author Contributions: Methodology, J.L.; software, G.Z.; writing—original draft preparation, H.L. (Huaying Li) and L.G.; writing—review and editing, L.G. and Y.S.; project administration, L.M. and H.L. (Haitao Liu). All authors have read and agreed to the published version of the manuscript.

Funding: This research was supported by Natural Science Foundation of Liaoning Province (2019-KF-25-05), Science and Technology Innovation Project of Educational Commission of Shanxi Province (No. 2020L0333), Excellent Innovation Project for Graduate students in Shanxi Province (2021Y666), the National Key Research and Development Program of China (2018YFB1308700).

Institutional Review Board Statement: Not applicable.

Informed Consent Statement: Not applicable.

Data Availability Statement: Not applicable.

Conflicts of Interest: The authors declare no conflict of interest.

References

1. Liu, Y.; Yang, J.J.; Yang, H.; Li, K.M.; Qiu, Y.T.; Zhang, W.C.; Zhou, S.F. Cu-bearing 316L stainless steel coatings produced by laser melting deposition: Microstructure and corrosion behavior in simulated body fluids. *Surf. Technol.* **2016**, *45*, 134–139.
2. Wang, Q.; Ren, L.; Li, X.P.; Zhang, S.Y.; Sercombe, T.B.; Yang, K. Antimicrobial Cu-bearing stainless steel scaffolds. *Mater. Sci. Eng. C* **2016**, *68*, 519–522.
3. Zhao, Z.Y.; Bai, P.K.; Misra, R.D.K.; Dong, M.Y.; Guan, R.G.; Li, Y.; Zhang, J.; Tan, L.; Gao, F.; Ding, T.; et al. AlSi10Mg alloy nanocomposites reinforced with aluminum-coated graphene: Selective laser melting, interfacial microstructure and property analysis. *J. Alloy. Compd.* **2019**, *792*, 203–214.
4. Rana, R.; Massardier, V.; Singh, S.B.; Mohanty, O.N. Effect of Pre-Treatment on Copper Precipitation Characteristics in a Copper-Alloyed Interstitial Free Steel Studied by Thermoelectric Power Measurement. *Metall. Mater. Trans. A* **2013**, *44*, 186–200.
5. Mcguire, M.F. *Stainless Steels for Design Engineers*; ASM International: New York, NY, USA, 2008.
6. Hong, I.T.; Koo, C.H. Antibacterial properties, corrosion resistance and mechanical properties of Cu-modified SUS 304 stainless steel. *Mater. Sci. Eng. A* **2005**, *393*, 213–222.
7. Monzen, R.; Iguchi, M.; Jenkins, M.L. Structural changes of 9R copper precipitates in an aged Fe-Cu alloy. *Philos. Mag. Lett.* **2000**, *80*, 137–148.
8. Liu, R.; Memarzadeh, K.; Chang, B.; Zhang, Y.M.; Ma, Z.; Allaker, R.P.; Ren, L.; Yang, K. Antibacterial effect of copper-bearing titanium alloy (Ti-Cu) against *Streptococcus mutans* and *Porphyromonas gingivalis*. *Sci. Rep.* **2016**, *6*, 29985.
9. Li, X.C.; Liu, J.; Zhu, W.X.; Tang, Y.C.; Wang, X.L. Research on Preventing Copper-Brittleness Process for Hot Rolling Copper-Containing of Atmospheric Corrosion-Resisting Steel Used in Vehicles. *Adv. Mater. Res.* **2014**, *1049–1050*, 27–30.
10. Huang, H.Q.; Di, H.S.; Yan, N.; Zhang, J.C.; Deng, Y.G.; Misra, R.D.K.; Li, J.P. Hot Deformation Behavior and Processing Maps of a High Al-low Si Transformation-Induced Plasticity Steel: Microstructural Evolution and Flow Stress Behavior. *Acta Metall. Sin.* **2018**, *31*, 503–514.
11. Montheillet, F.; Thomas, J.P. Dynamic Recrystallization of Low Stacking Fault Energy Metals. In *Metallic Materials with High Structural Efficiency*; Springer: Dordrecht, The Netherlands, 2004; pp. 357–368.
12. Yanushkevich, Z.; Belyakov, A.; Kaibyshev, R. Microstructural evolution of a 304-type austenitic stainless steel during rolling at temperatures of 773–1273 K. *Acta Mater.* **2015**, *82*, 244–254.

13. Gao, J.B.; Liu, J.; Wang, X.J.; Group, S. Microstructure Evolution of 304L Stainless Steel During Hot Deformation. *Foundry Equip. Technol.* **2014**, *2*, 45–47.
14. Mataya, M.C.; Nilsson, E.R.; Brown, E.L.; Krauss, G. Hot working and recrystallization of as-cast 317L. *Metall. Mater. Trans. A* **2003**, *34*, 1683–1703.
15. Qin, F.M.; Zhu, H.; Wang, Z.; Zhao, X.; He, W.W.; Chen, H.Q. Dislocation and twinning mechanisms for dynamic recrystallization of as-cast Mn18Cr18N steel. *Mater. Sci. Eng. A* **2017**, *684*, 634–644.
16. Yang, K.; Dong, J.S.; Chen, S.H.; Lu, M. The craftwork performance and resistance to corrosion of the Cu-containing antibacterial stainless steels. *Chin. J. Mater. Res.* **2006**, *20*, 523–527.
17. Li, J.; Zhao, G.H.; Chen, H.Q.; Huang, Q.X.; Ma, L.F.; Zhang, W. Hot deformation behavior and microstructural evolution of as-cast 304L antibacterial austenitic stainless steel. *Mater. Res. Express* **2018**, *5*, 025405.
18. Li, J.; Zhao, G.H.; Ma, L.; Chen, H.Q.; Huang, Q.X.; Zhang, W. Hot Deformation Behavior and Microstructural Evolution of Antibacterial Austenitic Stainless Steel Containing 3.60% Cu. *J. Mater. Eng. Perform.* **2018**, *27*, 1847–1853.
19. Li, J.; Zhao, G.H.; Ma, L.F.; Chen, H.Q.; Li, H.Y.; Zhang, W. Effect of copper element on hot behavior of 304L stainless steel. *Mater. Tehmol.* **2018**, *52*, 529–536.
20. Sharma, A.; Kumar, S.A.; Kushvaha, V. Effect of aspect ratio on dynamic fracture toughness of particulate polymer composite using artificial neural network. *Eng. Fract. Mech.* **2020**, *228*, 106907.
21. Sharma, A.; Kushvaha, V. Predictive modelling of fracture behaviour in silica-filled polymer composite subjected to impact with varying loading rates using artificial neural network. *Eng. Fract. Mech.* **2020**, *239*, 107328.
22. Kushvaha, V.; Kumar, S.A.; Madhushri, P.; Aanchna, S. Artificial neural network technique to predict dynamic fracture of particulate composite. *J. Compos. Mater.* **2020**, *54*, 3099–3108.
23. Cemernek, D.; Cemernek, S.; Gursch, H.; Pandeshwar, A.; Leitner, T.; Berger, M.; Klosch, G.; Kern, R. Machine learning in continuous casting of steel: A state-of-the-art survey. *J. Intell. Manuf.* **2021**, 1–19.
24. Majid, A.S.; Dominik, B.; Michael, E.; Mario, F.; Frank, M. Advanced Steel Microstructural Classification by Deep Learning Methods. *Sci. Rep.* **2018**, *8*, 2128.
25. Ballo, P.; Kioussis, N.; Lu, G. Grain boundary sliding and migration: Effect of temperature and vacancies. *Phys. Rev. B* **2001**, *64*, 167–173.
26. Wang, W.; Brisset, F.; Helbert, A.L.; Solas, D.; Drouelle, I.; Mathon, M.H.; Baudin, T. Influence of stored energy on twin formation during primary recrystallization. *Mater. Sci. Eng. A* **2014**, *589*, 112–118.
27. Wang, X.; Wang, D.; Jin, J.; Li, J. Effects of strain rates and twins evolution on dynamic recrystallization mechanisms of austenite stainless steel. *Mater. Sci. Eng.* **2019**, *761*, 138044.
28. Azarbarmas, M.; Aghaie-Khafri, M.; Cabrera, J.M.; Calvo, J. Dynamic recrystallization mechanisms and twinning evolution during hot deformation of Inconel 718. *Mater. Sci. Eng. A* **2016**, *678*, 137–152.
29. Shterner, V.; Timokhina, I.B.; Rollett, A.D.; Beladi, H. The Role of Grain Orientation and Grain Boundary Characteristics in the Mechanical Twinning Formation in a High Manganese Twinning-Induced Plasticity Steel. *Metall. Mater. Trans. A* **2018**, *49*, 2597–2611.
30. Xu, D.M.; Li, G.Q.; Wan, X.L.; Misra, R.D.K.; Yu, J.X.; Xu, G. On the deformation mechanism of austenitic stainless steel at elevated temperatures: A critical analysis of fine-grained versus coarse-grained structure. *Mater. Sci. Eng. A* **2020**, 773.
31. Eghbali, B. Effect of strain rate on the microstructural development through continuous dynamic recrystallization in a microalloyed steel. *Mater. Sci. Eng. A* **2010**, *527*, 3402–3406.
32. Marchattiwari, A.; Sarkar, A.; Chakravartty, K.J.; Kashyap, B.P. Dynamic Recrystallization during Hot Deformation of 304 Austenitic Stainless Steel. *J. Mater. Eng. Perform.* **2013**, *22*, 2168–2175.
33. Dehghan-Manshadi, A.; Barnett, M.R.; Hodgson, P.D. Recrystallization in AISI 304 austenitic stainless steel during and after hot deformation. *Mater. Sci. Eng. A* **2008**, *485*, 664–672.
34. Kapoor, R.; Nemat-Nasser, S. Determination of temperature rise during high strain rate deformation. *Mech. Mater.* **1998**, *27*, 1–12.
35. Wu, X. Research on High-Temperature Physical Properties and Mechanical Properties of Stainless Steel. Master's Thesis, Lanzhou University of Technology, Lanzhou, China, 2010.
36. Zhang, J.; Di, H.; Wang, X. Flow softening of 253 MA austenitic stainless steel during hot compression at higher strain rates. *Mater. Sci. Eng. A* **2016**, *650*, 483–491.
37. Pinheiro, I.P.; Barbosa, R.; Cetlin, P.R. The relevance of dynamic recrystallization in the hot deformation of IF steel at high strain rates. *Mater. Sci. Eng. A* **2007**, *457*, 90–93.
38. Liu, Y.; Hu, R.; Li, J.; Kou, H.; Li, H.; Chang, H. Deformation characteristics of as-received Haynes230 nickel base superalloy. *Mater. Sci. Eng. A* **2008**, *497*, 283–289.
39. McQueen, H.J.; Ryan, N.D. Constitutive analysis in hot working. *Mater. Sci. Eng. A* **2002**, *322*, 43–63.
40. Song, Y.H.; Wang, S.; Zhao, G.H.; Li, Y.G.; Li, J.; Zhang, J. Hot deformation behavior and microstructural evolution of 2205 duplex stainless steel. *Mater. Res. Express* **2020**, *7*, 046510.
41. Wang, K.; Wen, D.X.; Li, J.J.; Zheng, Z.Z.; Xiong, Y.B. Hot deformation behaviors of low-alloyed ultrahigh strength steel 30CrMnSiNi2A: Microstructure evolution and constitutive modeling. *Mater. Today Commun.* **2021**, *26*, 102009.